Journal of Volcanology and Geothermal Research 422 (2022) 107455

Contents lists available at ScienceDirect

Journal of Volcanology and Geothermal Research

journal homepage: www.elsevier.com/locate/jvolgeores

Decoding the plumbing system of Nevados de Chillán Volcanic complex, Southern Andes

Andrés Oyarzún [a,*], Luis E. Lara [b,c], Andrés Tassara [a,d]

[a] Departamento de Ciencias de la Tierra, Universidad de Concepción, Victor Lamas 1290, Concepción, Chile
[b] Servicio Nacional de Geología y Minería, Avenida Santa María 0104, Santiago, Chile
[c] Research Center for Integrated Disaster Risk Management (CIGIDEN), Avenida Vicuña Mackenna 4860, Santiago, Chile
[d] Millennium Nucleus The Seismic Cycle along Subduction Zones (CYCLO), Universidad de Concepción, Victor Lamas 1290, Concepción, Chile

ARTICLE INFO

Article history:
Received 10 February 2021
Received in revised form 9 December 2021
Accepted 13 December 2021
Available online 17 December 2021

Keywords:
Chilean Southern volcanic zone
Nevados de Chillán volcanic complex
Plumbing system
P-T estimation
Crustal geological discontinuities

ABSTRACT

Eruptions pose a threat to local and global communities and hence mitigation of the impact is required for a sustainable development. An extended knowledge of the plumbing system beneath volcanoes is key to assess volcanic hazards through a correct interpretation of the geophysical signals detected by monitoring networks. However, many volcanoes lack detailed studies that provide geophysical and/or petrological constrains for their plumbing systems. One of them is the Nevados de Chillán Volcanic Complex (NdCVC) in Southern Andes, which reawakened in January 2016 escalating from isolated explosions to lava emission that continues at the time of writing (December 2021). In this context, our aim is to constrain the architecture of the NdCVC plumbing system by means of petrological tools and provide insights for a more comprehensive interpretation of magmatic processes and ultimately the geophysical signals recorded at monitoring stations. In this study, mineral-melt equilibrium thermobarometry was performed for clinopyroxenes, orthopyroxenes and plagioclases included in volcanic rocks. Our thermobarometric results suggest that the NdCVC plumbing system extends vertically from ca. 2 to 17 km depth. The depth of crystallization for mineral phases included in basaltic andesites/andesites matches the intracrustal Conrad discontinuity in this area, while evolved magmas migrate and store above this level, which in turn suggests a compositionally zoned plumbing system. Our results highlight the first-order role played by crustal geological discontinuities in the configuration of a plumbing system, despite the concomitant role that external forcings as crustal tectonics may play.

1. Introduction

Eruptions pose a threat to local and global communities and hence mitigation of their impact is required for a sustainable development. In coping with volcanic hazards and risks, early warning systems and instrumental monitoring networks are essential. However, the analysis of geophysical data requires an extended knowledge of the plumbing systems allowing for a correct interpretation of the signals and time series (e.g., Aiuppa et al., 2010; Kahl et al., 2011). In fact, conceptual models of plumbing systems constrained by petrology are useful to better understand patterns of seismicity and deformation observed in volcanoes under unrest, which usually show different patterns depending on the geological context (e.g., Sigmundsson et al., 2018). However, many volcanoes lack detailed studies that provide geophysical and/or petrological constrains for the architecture of their plumbing systems. One of them is Nevados de Chillán Volcanic Complex in Southern Andes, which reawakened in January 2016 (Moussallam et al., 2018; Benet et al., 2021; Cardona et al., 2021), escalating from isolated explosions to lava emission that continues at the time of writing (www.sernageomin.cl).

Currently, plumbing systems are imagined as vertically-zoned with multiple levels of magma ponding and subsequent differentiation (Gilbert et al., 2012; Annen et al., 2015; Sparks and Cashman, 2017). Factors controlling such a complex structure are density contrasts between magma and crustal rocks and the inherent discontinuities of the lithosphere, which express themselves in temperature and elastic properties changing over the crustal column (e.g., Valentine and Krogh, 2006; Kavanagh et al., 2006; Menand, 2008). The well-known Moho (crust-mantle boundary) and the Conrad (intracrustal) discontinuity, are hence thought to be playing a role in the transit and storage of magmas (e.g., Annen and Sparks, 2002; Kavanagh et al., 2006).

In this context, interpretation of the seismic signals carries some ambiguity and affect the quality of hazards assessment. We select Nevados de Chillán Volcanic Complex as a case-study because of both the present activity that deserves attention and the availability of a large number of

* Corresponding author.
E-mail address: aoyarzun@udec.cl (A. Oyarzún).

https://doi.org/10.1016/j.jvolgeores.2021.107455
0377-0273/

samples from different geological units, which provide an opportunity to test petrological tools and assess the stability of the plumbing system over time. Our aim is to constrain the geometry of the plumbing system and provide insights for a more comprehensive interpretation of magmatic processes and ultimately the geophysical signals recorded by the monitoring networks.

2. Geological setting

Nevados de Chillán Volcanic Complex (NdCVC) is located in the Southern Andean Volcanic Zone (SVZ), right on the transition from a thick (>50 km) subarc continental crust in the north to a thin (<40 km) crust southward (López-Escobar et al., 1993; Stern, 2004; Tassara and Echaurren, 2012). The NdCVC is ranked fourth by the Chilean Geological Survey (Sernageomin) in terms of hazards and exposure (www.sernageomin.cl) and also scored high in other hazards classification schemes (e.g., Lara et al., 2021).

The NdCVC has an elevation that exceeds 3100 m.a.s.l with a height of 1000–1250 m (Naranjo et al., 2008) and overlies a ca. 1000 m thick basement (Folguera et al., 2006) formed by a subhorizontal sequence of Pliocene to Early Pleistocene volcanic rocks (Cola de Zorro Formation; González and Vergara, 1962; Vergara and Muñoz, 1982). The Cola de Zorro Formation overlies folded Cenozoic volcano–sedimentary rocks (Cura-Mallin Formation) that form a cover at least 2500 m thick (Radic, 2010) above the crystalline basement. The continental crust is ca. 40 km thick at this latitude and is vertically segmented with the intracrustal Conrad discontinuity (ICD) at a depth of ca. 8 km b.s.l (Tassara and Echaurren, 2012).

NdCVC is composed of two main volcanic edifices (Cerro Blanco and Las Termas; Dixon et al., 1999) that host 13 eruptive centers forming a NW-striking alignment ca. 16 km long (Fig. 1). The volcanic edifices are separated by a saddle region with three eruptive centers (Pichicalfú, Baños and Shangri-La units; Dixon et al., 1999; Naranjo et al., 2008). Two Holocene scoria cones, Las Lagunillas y Parador, are located on the eastern and western flanks respectively, ca. 5 km away from the main edifices.

The NdCVC eruptive history started around 640 ka with the eruption of thick and extensive sub-glacial andesitic lava flows (Naranjo et al.,

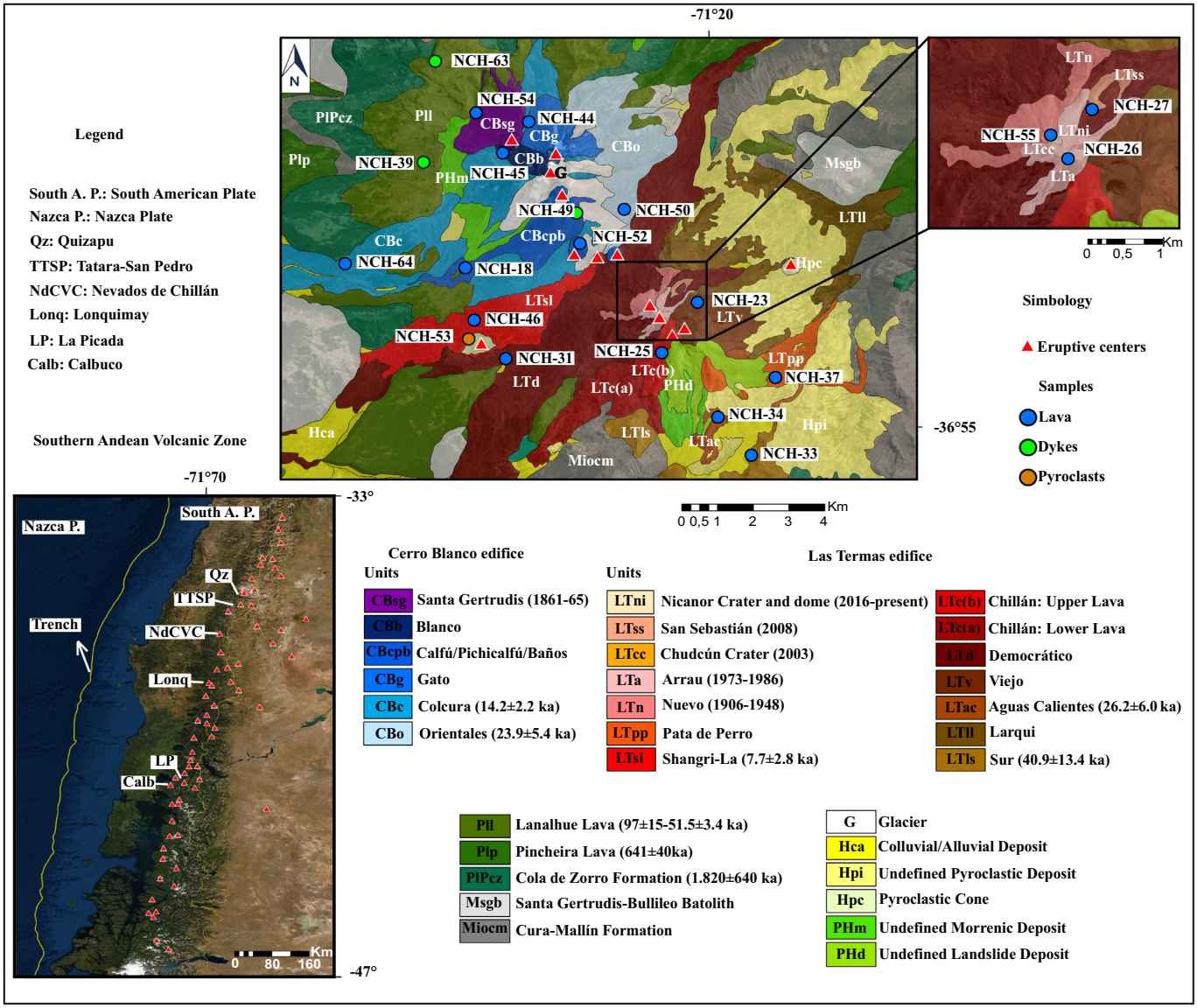

Fig. 1. Simplified geological Map of Nevados de Chillán Volcanic Complex (NdCVC) from Naranjo et al. (2008). The modern composite NdCVC is formed since the last ca. 40 ka by two volcanic edifices; Cerro Blanco and Las Termas. Cura-Mallín Formation, Cola de Zorro Formation and Santa Gertrudis-Bullileo Batolith are part of the NdCVC basement. The radiometric ages are taken from Dixon et al. (1999), Mee (2004, 2009) and Naranjo et al. (2008). Circles show the location of samples collected for chemical analysis in this study and red triangles show the location of eruptive centers. (For interpretation of the references to colour in this figure legend, the reader is referred to the web version of this article.)

2008). From ca. 640–50 ka, sub-glacial andesitic lavas predominate including Pincheira, Atacalco, Diguillín and Lanalhue units (Naranjo et al., 2008), which form the basement for the composite modern edifice (Dixon et al., 1999; Naranjo et al., 2008). Around 40 ka, deposits of non-welded pyroclastic density currents and ash, pumice and scoria layers fall deposits were emplaced from eruptions that possibly correlate with a caldera formation event (Dixon et al., 1999), although evidence for that is still scarce. These deposits form a succession named as El Castillo ignimbrites (Naranjo et al., 2008), which have been correlated with the extensive ignimbrites recognized up to 100 km west-northwest of the NdCVC (Varela and Moreno, 1982; Naranjo and Lara, 2004). After this major explosive event, the development of the present edifices began.

In the Cerro Blanco edifice (CB) the andesitic compositions predominate and the eruptive activity began at ca. 24 ka (Orientales unit; Dixon et al., 1999; Naranjo et al., 2008). During the Holocene the eruptive products have been emitted from different eruptive centers (Colcura, Gato, Blanco, Calfú units; Dixon et al., 1999; Naranjo et al., 2008) and the last eruption occurred in the 1861–1865 period (Santa Gertrudis unit; Dixon et al., 1999; Naranjo et al., 2008). More evolved compositions dominate the edifice of Las Termas (LT), except for some andesitic lavas (Sur, Democrático and upper Chillán units; Dixon et al., 1999; Naranjo et al., 2008). Its eruptive activity also began at ca. 40 ka with an andesitic lava sequence (Sur unit) followed by dacitic lavas (Aguas Calientes unit; ca. 30 ka), all of them with ice-contact features (Dixon et al., 1999; Naranjo et al., 2008). In the post-glacial period, the eruptive products were also emitted from different eruptive centers (Democrático, Viejo, Chillán, Pata de Perro, Nuevo, Arrau, Chudcún, San Sebastián and Nicanor). Holocene tephra fall deposits crop-out to the east and south of NdCVC being geochemically correlated with Viejo and Calfú eruptive centers (Dixon et al., 1999).

In the last century, volcanic activity has been concentrated in Las Termas edifice with a relatively uniform dacitic composition of the eruptive products. The largest (and longer) historical eruptions occurred in 1906–1948 (Nuevo unit) and 1973–1986 (Arrau unit) with a minor Vulcanian episode in 2003 (Chudcún crater; Naranjo and Lara, 2004) and a gently effusive eruption in 2008 (San Sebastián unit; Coppola et al., 2016), both sourced from an area between the Nuevo and Arrau craters. The latter is also the vent area for the current eruption (Nicanor crater and dome), which started in 2016 (Moussallam et al., 2018; Benet et al., 2021; Cardona et al., 2021) as weak explosions that became stronger and culminated with magma extrusion in January 2018 forming a series of small domes that feed a lava flow on the south-western slope.

The NdCVC magmatic evolution has been qualitatively discussed and can be understood by three main processes: fractional crystallization, magma mixing and assimilation of continental crust (Murphy, 1995). Differences in the content of some trace elements of the more evolved and the less differentiated rocks are probably due to different parents and/or fractionation histories (Murphy, 1995). Compositional differences are also observed between volcanic edifices and are thought to result from different residence times of the magmas within the crust (Dixon et al., 1999). The CB system would have been replenished more frequently than LT promoting a higher eruptive frequency, which in turn might be a consequence of the local basement structure (Dixon et al., 1999).

A remarkable feature of NdCVC is the NW-striking alignment of eruptive centers, which is related to the regional-scale basement structure making this a case of basement-controlled volcanic clusters (Cembrano and Lara, 2009). Radic (Radic and Sipetrol, 2006; Radic, 2010) proposed that former normal faults connecting depocenters of the extensional Oligo-Miocene basins were inverted in the Upper Miocene to define the present structure. It has also been proposed that NdCVC developed upon the prolongation of the NW- trending Cortaderas lineament (e.g., Stanton-Yonge et al., 2016; González-Vidal et al., 2018), which would be a crustal-scale discontinuity now better exposed in the back-arc region (Hernando et al., 2012; Søager et al., 2013). Despite the nature of the basement anisotropy, the distribution of shear wave velocities beneath the NdCVC (González-Vidal et al., 2018) seems to confirm a NW-striking pattern, which is also illuminated by the present seismicity (Cardona et al., 2021).

3. Material and methods

3.1. Sampling and petrographic study

Fifty representative samples of post-caldera Pleistocene-Holocene lava flow units, three dykes (NCH-49, NCH-39 and NCH-63) and a tephra sample from a pyroclastic cone (NCH-53), were collected during two field campaigns (2018, 2019). Thirty polished thin sections were described petrographically with an optical microscope and fifteen with BSE (backscattered electron) images obtained by electron microprobe. The modal percentages of mineral phases, groundmass and plagioclase types (according to their textures) of fourteen representative lavas samples and the three dykes were determined using a controlled stage and a counter (1000 points per section). The crystals smaller than 100 μm were considered as part of the groundmass.

3.2. Whole-rock and mineral chemistry

Major and trace element concentrations of whole-rock for 22 samples, were acquired at ACME Laboratories (Canada). Whole-rock analyses were performed by inductively coupled plasma-emission spectrometry ICP-ES (major elements) and inductively coupled plasma–mass spectrometry ICP-MS (trace elements). The results and Method Detection Limits (MDLs) for all major oxides and trace elements are listed in Supplementary Material. Accuracy of the methods was confirmed by internal reference materials (SO-19 for major and trace elements) and duplicates. In addition, in this study we use as reference the major and trace element concentrations of 85 samples obtained from Murphy (1995), Dixon et al. (1999), Deruelle and López-Escobar (1999) and Mee et al. (2009). Since the FeO total is usually reported as FeO_t or $Fe2O3_t$ in previous contributions, it was necessary to estimate the proportions of both cations for each sample, and to calculate the FeO total accordingly. These ratios were obtained from the concentrations of both oxides for different volcanic rocks as proposed by Middlemost (1989).

Pyroxene, plagioclase, olivine and Fe-Ti oxides core-rim compositions (Supplementary Material) were obtained by wavelength-dispersive spectrometry (WDS) using the electron microprobe (JEOLJXA-8600 M Superprobe) at Universidad de Concepción (Chile) and Rice University (USA; JEOLJXA 8530F Hyperprobe). Analyses were carried out using standard operating conditions of 15 kV accelerating voltage and 20 nA beam current and a spot size of 3 μm was used for the all analyses with exception of plagioclase, for which the beam size was set to 10 μm beam diameter to avoid Na and K loss during sample-beam interaction. More details of the analytical conditions are given in Supplementary Material.

4. Results

4.1. Geochemistry

Based on the entire geochemical dataset (this study and previous data) the NdCVC lavas range from basaltic andesite to rhyolite, between 53.1 and 70.6 wt% SiO_2 (volatile-free normalization; Fig. 2). The mineral phases present are plagioclase (Pl), clinopyroxene (Cpx), orthopyroxene (Opx), olivine (Ol), Fe-Ti oxides (Ox), apatite and trace amounts of sulfides. Hydrated minerals such as amphiboles and biotites are absent (Table 1).

The SiO_2 content shows a negative correlation with Al_2O_3, FeOt, CaO, MgO, Sr, Sc, V, Co and Ni, and a positive correlation with K_2O, Na_2O, Rb,

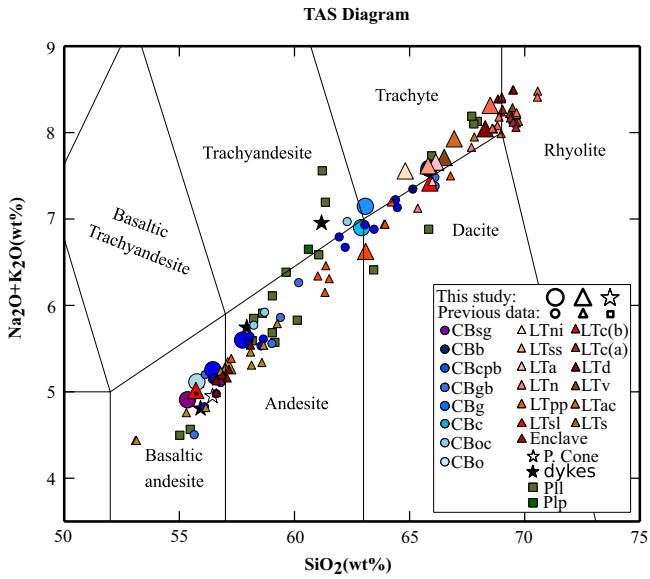

Fig. 2. Total alkali versus silica diagram. (TAS; Bas et al., 1986) for NdCVC samples. The compositions span from basaltic andesite to rhyolite for all samples. Largest circles, triangles and stars show the data from this study (mafic enclave in LTsl is represented by a black circle within a red triangle). Previous data (smaller symbols) were obtained from Murphy (1995), Dixon et al. (1999), Deruelle and López-Escobar (1999) and Mee et al. (2009). Data were normalized on a volatile-free basis. CB: Cerro Blanco edifice; LT: Las Termas edifice; P.cone: Pyroclastic cone. Pincheira, and Lanalhue lavas were emitted prior to the development of the two volcanic edifices. (For interpretation of the references to colour in this figure legend, the reader is referred to the web version of this article.)

Ba, Y, Zr, Hf, Nb, Th and REE. For TiO_2 and P_2O_5, SiO_2 shows a positive correlation up to ca. 60 wt% SiO_2, and then the correlation become negative. The observed variation in major oxides and trace element (Figs. 3 and 4) is consistent with fractionation of calcic plagioclase, pyroxene, olivine at an early crystallization stage and dominantly sodic plagioclase, pyroxene, titanomagnetite/ilmenite and apatite in later stages. The TiO_2 and FeOt/MgO vs SiO_2 (wt%) diagrams (Fig. 3) show significant differences in samples with the same degree of differentiation. In general, samples that plot in the lower trend in TiO_2 and FeOt/MgO are those from Las Termas edifice that contain macroscopically distinguishable mafic enclaves. Hypothetical fractionation and mixing trends (Fig. 3) in TiO_2 and FeOt/MgO vs SiO_2 (wt%) were obtained from Murphy (1995) and Dixon et al. (1999). Other chemical differences in rocks with same SiO_2 content is probably due to different parents and/or fractionation histories.

Table 1
Mass fractions for representative NdCVC samples analyzed in this study.

Samples	SiO_2%[b]	Mass fraction (%)[a]						Plagioclase texture%		
		Pl	Cpx	Opx	Ol	Ox	Gms	Type 1	Type 2	Type 3
NCH-18	57.4	21.7	2.9	0.3	0.2	0.1	74.8	0	42	58
NCH-25	61.5	11.2	2.0	0.0	0.2	0.4	86.2	10	16	74
NCH-26	65.7	13.1	2.2	0.6	0.0	1.1	83.0	0	0	100
NCH-27	65.2	19.6	2.2	1.0	0.0	1.6	75.5	0	4	96
NCH-31	67.8	4.2	0.2	0.2	0.0	0.2	95.2	0	0	100
NCH-33	56.8	19.6	4.0	1.0	0.0	0.0	75.4	28	29	43
NCH-34	66.3	7.6	0.9	0.1	0.0	0.9	90.5	0	0	100
NCH-37	68.0	8.0	0.2	0.1	0.0	0.4	91.3	0	0	100
NCH-39	60.3	2.1	0.4	0.2	0.0	0.0	97.3	0	0	100
NCH-44	62.8	5.2	0.9	0.6	0.0	0.8	92.5	0	8	92
NCH-45	65.5	13.7	1.7	0.6	0.0	1.4	82.6	0	5	95
NCH-46	65.6	11.8	2.5	0.1	0.9	0.6	84.1	14	12	74
NCH-49	54.9	20.2	2.4	0.0	0.0	0.0	77.4	28	40	33
NCH-50	55.3	23.0	1.7	0.0	3.7	0.0	71.5	0	88	12
NCH-54	55.3	28.8	5.9	0.0	0.0	0.1	65.2	4	0	96
NCH-55	64.4	16.1	0.7	0.4	0.0	1.2	81.5	0	2	98
NCH-63	57.0	3.4	0.6	0.0	0.0	0.0	96.0	0	65	35

Abbreviations: Pl, Plagioclase; Cpx, Clinopyroxene; Opx, Orthopyroxene; Ol, Olivine; Ox: Fe-Ti oxides; Gms, Groundmass. The types of plagioclases are explained in the text.
[a] Estimated from point counting data (1000 points per sample). Apatite was not considered, but their occurrence increases with differentiation. Trace amounts of sulfides are also observed.
[b] Whole rock analyses.

4.2. Petrography and mineral chemistry

Modal analyses for selected samples, many of which have been analyzed with microprobe, are given in Table 1. Mineral compositions are listed in the Supplementary Material. For the plagioclase, the anorthite content was calculated as the molar ratio Ca/(Ca + Na + K) and is reported as mol %. For the pyroxene and olivine, the Mg-number (Mg#) and the forsterite content (Fo), were calculated as the molar ratio Mg/(Mg + Fe) both being reported as a percentage.

Lavas and dykes analyzed have a phenocrysts content between 3 and 35 vol% (normalized to vesicle-free, Table 1). Often the phenocrysts are present as individual grains, but clusters of plagioclases and clots of plagioclases, pyroxenes and/or Fe-Ti oxides and/or apatite also are observed. The biggest crystals are usually included in crystal clots. The groundmass is commonly hypocrystalline and trachytic, to a lesser extent intersertal, and is generally composed of glass and crystals of plagioclases, pyroxenes and Fe-Ti oxides.

Plagioclase is the most abundant mineral phase in all samples (Table 1), either as individual grains or forming clots with other minerals. They are commonly euhedral to subhedral, presenting three main types of textures and in some cases all three types are observed in the same sample (Table 1): Type 1 with fine sieve or dusty texture, given by the intergrowth of plagioclase and glass mainly confined in the rims of the plagioclases (Fig. 5a); Type 2 usually larger crystals with coarse sieve texture given by large melts inclusions mainly in the core (Fig. 5b) and, usually accompanied of patchy and; Type 3 without melts inclusions. The latter is the most abundant, with no zoning or showing normal or reverse oscillatory zoning and, in some cases, dissolution/reabsorption textures (Fig. 5c). Type 1 textures reflect major dissolution boundaries of the resorbed plagioclase and are commonly attributed to episodes of magma mixing (e.g., Tsuchiyama, 1985; Tepley III et al., 1999). Type 2 textures may occur by rapid decompression when the P (H_2O) of the system increases reducing the stability of plagioclase and causing dissolution (Nelson and Montana, 1992; Blundy and Cashman, 2001; Humphreys et al., 2006). In basaltic andesites and andesites the sizes of the phenocrysts of plagioclases range between 0.15 and 2.0 mm and have a compositional range in the core between An_{51-80} and in the rim of An_{43-67}. In dacites and rhyodacites the sizes range between 0.15 and 1.5 mm and the composition in the core ranges from An_{39-73} and the rim between An_{32-57}.

Pyroxenes are euhedral to subhedral and occur usually without zoning or with reverse and normal zoning (Supplementary Material), but some pyroxenes present patchy zoning texture in the whole crystal. Clinopyroxenes are the second most abundant mineral phase and are present in all samples analyzed (Table 1). The orthopyroxenes increase their proportion with the differentiation. In basaltic andesites and andesites the sizes of the phenocrysts of pyroxenes range between 0.1 and 0.7 mm and have a compositional range in the core between $Mg\#_{72-81}$ and in the rim of $Mg\#_{68-76}$. Orthopyroxenes (0.05–0.6 mm in size) are unzoned or with a magnesium-rich rim and the core composition ranges between $Mg\#_{68-73}$ and the rim between $Mg\#_{66-75}$. In dacites and rhyodacites the clinopyroxenes the sizes range between 0.1 and 0.6 mm and the core ranges between $Mg\#_{65-81}$ and the rim between $Mg\#_{62-78}$ and the orthopyroxenes (0.1–0.7 mm in sizes) range between $Mg\#_{58-70}$ in the core and between $Mg\#_{56-74}$ in the rim.

Olivines are usually found in the less differentiated rocks and mafic enclaves. Olivine phenocrystals (2–3 mm in size) occur as individual

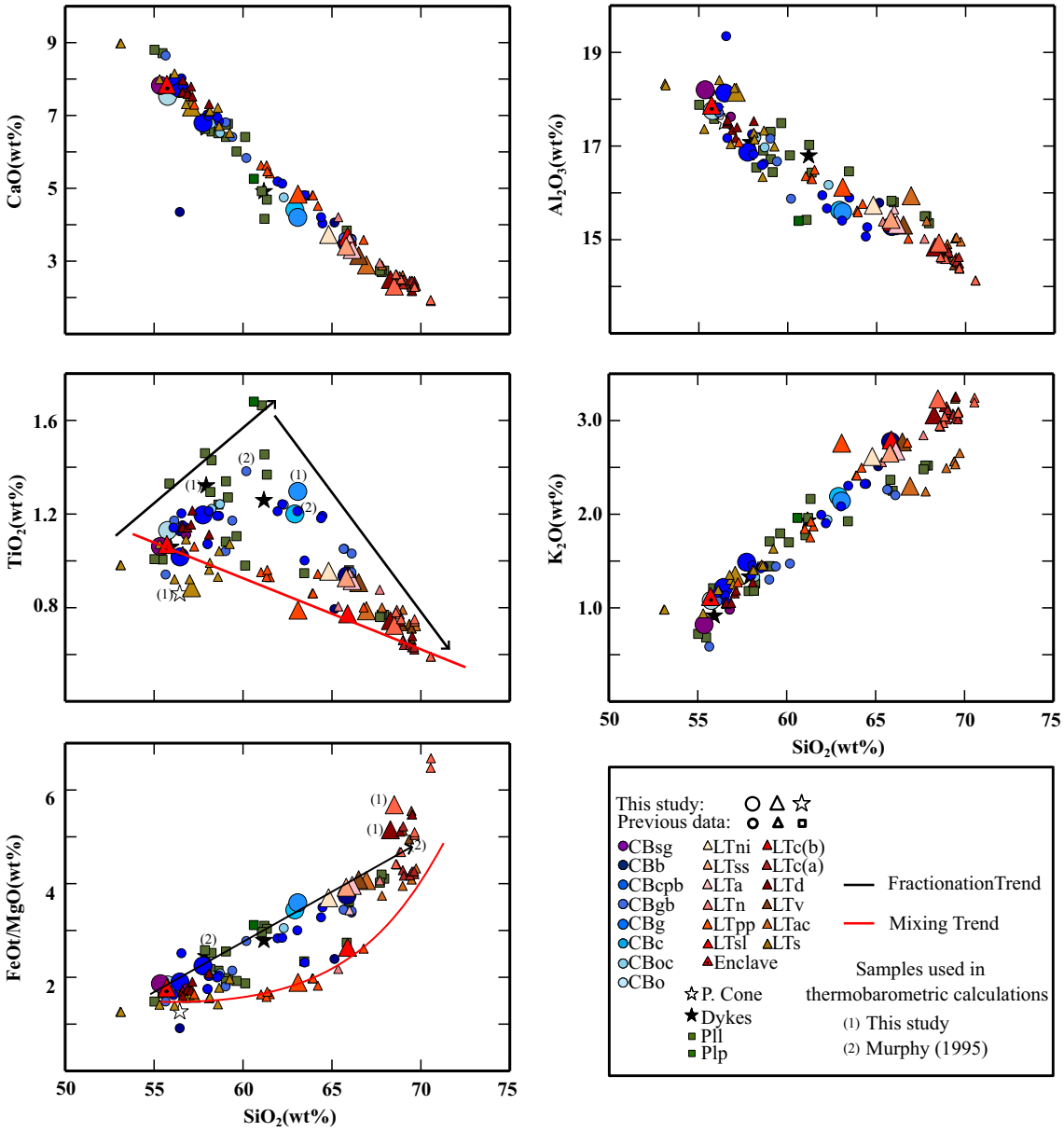

Fig. 3. Harker diagrams of CaO, Al_2O_3, TiO_2, K_2O and FeOt/MgO vs SiO_2 (wt%). The observed variation in these major element oxides is consistent with fractionation of calcic plagioclase, pyroxene, olivine and Fe-Ti oxides. Symbols as in Fig. 2. Hypothetical fractionation and mixing trend were obtained from Murphy (1995) and Dixon et al. (1999). Numbers in parentheses indicate the samples used in thermobarometric estimates: (1) samples from this study and (2) samples from Murphy (1995).

and rounded grains, unzoned and in some cases, with a rim of low Ca-pyroxenes. In NCH-18 two grains have Fo_{67-71} in the rim. In mafic enclaves (e.g., NCH-60), individual olivines grains are accompanied of phenocrysts of plagioclases, clinopyroxenes and orthopyroxenes set in a glassy, diktytaxitic groundmass (Fig. 5d). An individual olivine grain analyzed in a mafic enclave is zoned with Mg-rich core (Fo_{84}) and more iron-rich rim (Fo_{77}). Some lavas (e.g., NCH-46, NCH-25, NCH-34) contain mafic enclaves reaching 30 cm in diameter and rounded grains of olivine crystals are also observed in the dacitic part of these lavas, possibly due to disaggregation (e.g., Zellmer and Turenr, 2007; Ruprecht et al., 2020).

Fe-Ti oxides occur as small individual grains mainly in the groundmass or as inclusions within pyroxene and some plagioclase phenocrysts and increase their proportions with the differentiation. In NCH-31 small euhedral crystals of titanomagnetite range from Ulv_{50-54} and ilmenite from Ilm_{89-91}. Euhedral apatite occurs as small individual grains or as inclusions in plagioclases and pyroxenes and their proportion increase with the differentiation. Some small crystals of sulfides are found as inclusions in pyroxenes.

The mineral-melt equilibrium equations used for estimations of pressure and temperature of crystallization (Section 4.6), consider the whole-rock composition as representative of the melt, only when the content of crystals is ca. <10 vol%. Samples that show clear textural or compositional evidence of magma mixing (e.g., Type 1 plagioclase, presence of mafic enclaves or that fall into the hypothetical mixing trend; Fig. 3) were also discarded, because the composition of the whole-rock might not be representative of the melt in which the crystal grew.

Along with the general features described above, we use selected samples to show in detail textures and mineral compositions that support the extensive use of thermobarometers. Those samples were selected because they represent dominant lithologies recognized in the most conspicuous eruptive units, they are crystal-poor, without clear textural or compositional evidence of magma mixing and they have unzoned or weakly zoned crystals.

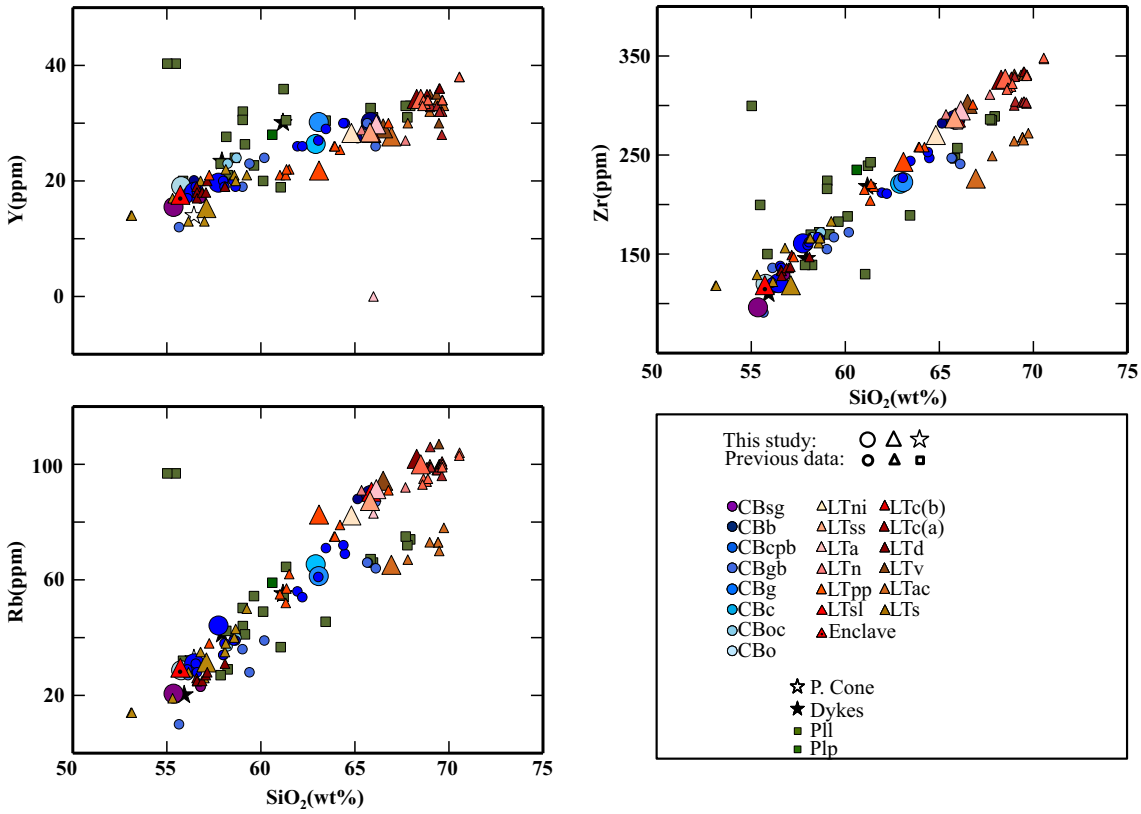

Fig. 4. Harker diagrams for some trace elements. Y, Zr and Rb (ppm) vs SiO_2 (wt%). Symbols as in Fig. 2.

NCH-31 (LTd, 67.8 wt% SiO_2)

This sample has a phenocryst content of 4.8 vol% (normalized to vesicle-free, Table 1). Phenocrysts of plagioclase and orthopyroxene predominate as individual grains, but clots of plagioclase, pyroxene, Fe-Ti oxide and apatite also are observed. Fe-Ti oxides (titanomagnetite > ilmenite) and apatite also occur as small individual grains mainly in the groundmass and as inclusions within pyroxene and plagioclase phenocrysts. The predominant texture of the groundmass is intersertal trachytic with plagioclase microlites, pyroxenes and Fe-Ti oxides. Only Type 3 plagioclases are present and eight individual grains were analyzed (Supplementary Material). The sizes of the euhedral to subhedral plagioclases range between 0.2 and 0.4 mm and they are relatively homogeneous in composition from core to rim with weakly oscillatory zoning (Fig. 5e). The oscillatory zoning in Type 3 plagioclases, without reabsorption and with fine banding, may be largely kinetically controlled (e.g., Ginibre et al., 2002; Humphreys et al., 2006). Plagioclase composition core ranges between An_{39-44}, except for a grain with core An_{50}, and the rim ranges between An_{39-43}. Two euhedral to subhedral clinopyroxenes analyzed have sizes of 0.1 mm and they are unzoned and weakly zoned. The composition in the core is $Mg\#_{66}$ and the rim ranges between $Mg\#_{65-66}$. Ten euhedral to subhedral orthopyroxenes analyzed have sizes between 0.05 and 0.2 mm and show subtle normal zoning. The core ranges between $Mg\#_{60-65}$, except for a grain with core $Mg\#_{70}$ and, the rim between $Mg\#_{58-62}$. Small euhedral crystals of titanomagnetite and ilmenite range from Ulv_{50-54} and from $Ilm_{89-91,}$ respectively.

NCH-37 (LTpp, 68.0 wt% SiO_2)

This sample has a phenocryst content of 8.7 vol% (normalized to vesicle-free, Table 1). The mineral phases and their occurrence are the same as in NCH-31 (Table 1), but with a higher proportion of plagioclase and Fe-Ti oxides (titanomagnetite > ilmenite). Clinopyroxenes usually occur in clots with plagioclases, orthopyroxenes, Fe-Ti oxides and apatite. The predominant texture of the groundmass is intersertal trachityc with plagioclase microlites, pyroxenes and Fe-Ti oxides. As in NCH-31, Only Type 3 plagioclases are present and six individual grains were analyzed (Supplementary Material). The plagioclases are euhedral to subhedral and their sizes range between 0.2 and 0.4 mm and they are relatively homogeneous in composition from core to rim con weakly oscillatory zoning. Plagioclase composition core ranges between An_{39-42}, except for a grain with core An_{51}, and the rim between An_{37-40}. One subhedral clinopyroxene analyzed has size of 0.3 mm and it is weakly zoned. The core ranges between $Mg\#_{66-67}$, and the rim has $Mg\#_{65}$. Six euhedral to subhedral orthopyroxenes analyzed have sizes between 0.1 and 0.3 mm and show subtle normal zoning (Fig. 5f). The core composition ranges between $Mg\#_{58-61}$ and the rim between $Mg\#_{56-60}$.

NCH-44 (CBg, 62.8 wt% SiO_2)

This sample has a phenocryst content of 7.5 vol% (normalized to vesicle-free, Table 1). Pyroxenes and plagioclases are usually euhedral to subhedral and occur as individual grains or in clots, often with titanomagnetite. Titanomagnetite also occurs as small individual grains mainly in the groundmass and as inclusions within pyroxene and plagioclase phenocrysts and in clots with those minerals. The predominant textures of the groundmass are hypocrystalline to trachytic with plagioclase microlites, pyroxenes and titanomagnetite. Type 3 plagioclases predominate (0.15–0.8 mm in size) with weakly oscillatory zoning in the whole crystal with a decrease of anorthite from core to rim (Supplementary Material). The composition of the plagioclases range in the core between An_{49-51} and the rim between An_{42-50}. The lowest values of anorthite were measured in the outermost part of the crystal and in some cases coincides with an increase in Fe/Al (Supplementary Material), which suggests oxidation as a result of degassing of H_2O during decompression (Humphreys et al., 2006). Nine clinopyroxenes

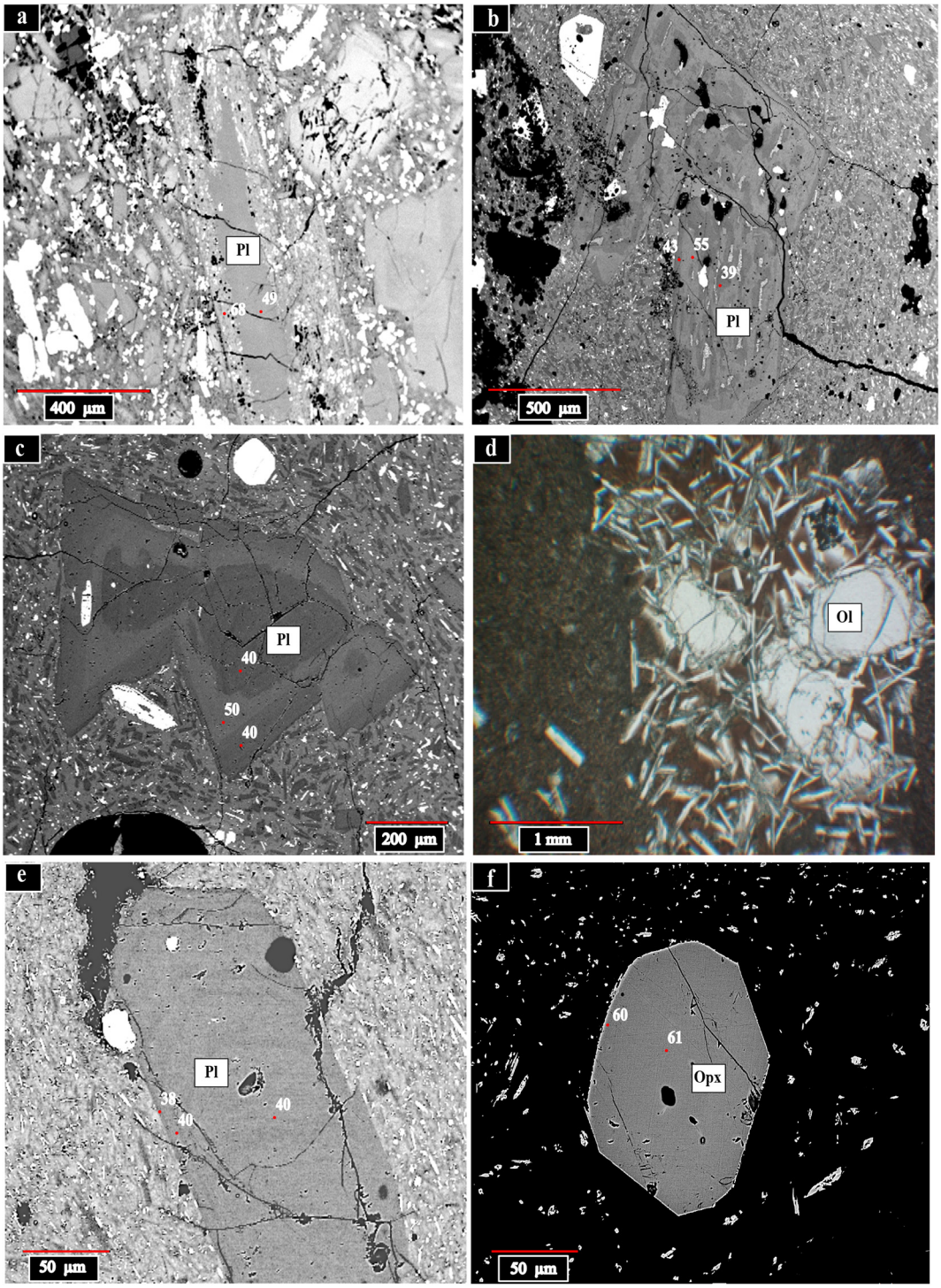

Fig. 5. (a) Type 1 plagioclase (Pl) with fine sieve texture in the rim; (b) Type 2 plagioclase (Pl) with coarse sieve texture in the core; (c) Type 3 plagioclase (Pl) with a partially anhedral resorbed anorthite-poor core; (d) Basaltic andesite enclave with phenocrysts of plagioclase and olivine (Ol) set in a glassy, diktytaxitic groundmass; (e) Type 3 plagioclase with weakly oscillatory zoning in NCH-31 and; (f) Orthopyroxene in NCH-37. (a), (b), (c), (e) and (f), BSE images taken with an electronic probe and (d) images from an optical microscope. Red circle: Anorthite and Mg# contents for plagioclase and orthopyroxene, respectively. (For interpretation of the references to colour in this figure legend, the reader is referred to the web version of this article.)

analyzed have sizes between 0.2 and 0.4 mm and they are generally unzoned or with subtle normal zoning, without major textural and compositional differences between phenocryst as individual grains or in the clots. The core ranges between $Mg\#_{73–74}$, and the rim between $Mg\#_{70–73}$. Nine orthopyroxenes analyzed have sizes between 0.1 and 0.4 mm and they are unzoned. The core and rim range between $Mg\#_{70–73}$.

4.3. Water content

To constrain the water content on select samples for thermobarometric calculations, we used the plagioclase-melt hygrometer of Waters and Lange (2015), with a standard error of estimate (SEE) ± 0.35 wt% H_2O. This hygrometer requires an estimate of the crystallization pressure but is relatively insensitive to this parameter.

Over the range of 100–900 MPa, the calculated water content varies by only 0.15 wt%. Therefore, calculations were made at a constant pressure of 3 kbar. This hygrometer also requires as input a value of the melt temperature. The temperature used in these calculations correspond to the lowest estimated temperature for clinopyroxenes with a thermobarometer independent of the water content (Putirka, 2008 in Putirka, 2008) for each sample (Table 2). In the case of the NCH-31 sample this temperature estimate is in agreement with the temperature calculated with Fe-Ti oxides (three pairs). Compositions of Fe-Ti oxide pairs that passed the Mg-Mn equilibrium test by Bacon and Hirschmann (1988) were used to estimate temperatures according to the method outlined in Ghiorso and Evans (2008). With these temperature values the estimated water content for NCH-31 is 3.0 wt%, NCH-37 of 3.1 wt% and 2.2 wt% for NCH-44, respectively. These water contents are lower than the values estimated with experimental and petrological studies in dacitic lavas of volcanic centers near the NdCVC. In Quizapu volcano these values are in the range 4–6 wt% (Ruprecht et al., 2012) and between 4.5 and 5.5 wt% at the San Pedro volcano (Costa et al., 2004), in which hydrated minerals such as amphibole are part of the mineral assemblage of these lavas. The absence of amphibole in NdCVC lavas would support lower water content estimates (e.g., Andújar et al., 2015; Sisson and Grove, 1993).

4.4. hermobarometry

In order to understand the configuration of the NdCVC plumbing system, we use selected samples to estimate the pressure and temperature of crystallization for the main mineral phases following Putirka (2008), which uses mineral-melt equilibrium equations. We consider in this study the whole-rock composition as representative of the melt assemblages for whole-rock–phenocryst rims (we only consider individual grains) when the content of crystals is <10 vol%.

Assessment of the mineral-melt equilibrium was carried out using the spreadsheet provided by Putirka (2008). In the case of clinopyroxenes and orthopyroxenes, the equilibrium was tested on the basis of the Fe/Mg partitioning between the melt (whole-rock) and mineral. To visualize this equilibrium test, the Rhodes diagram (Rhodes et al., 1979; Putirka, 2008) was used, where the Mg# of clinopyroxene is plotted versus the Mg# of whole-rock (Fig. 6a; Kd [Fe-Mg] = 0.27 ± 0.8). For orthopyroxenes (Fig. 6b; Kd [Fe-Mg] = 0.29 ± 0.6), we estimated the ratio Fe^{2+}/Fe_t in the melt. To obtain this value, we used the ratios between both oxides, for different volcanic rocks, proposed by Middlemost (1989). For plagioclase, the Kd [Ab-An] equilibrium test was used, based on the exchange of An-Ab between the melt/whole-rock and the mineral (Fig. 6c). To validate the equilibrium, this value of Kd [Ab-An] must be between 0.11 ± 0.5 for T° <1050 °C and between 0.27 ± 0.11 for T° >1050 °C (Putirka, 2008).

Thermobarometric equations were only applied to the mineral phases that passed the equilibrium test. For clinopyroxenes the temperature was estimated as in Purtirka (2003, in Putirka, 2008), with a standard error of estimate (SEE) ± 59 °C and the pressure with clinopyroxene barometer for hydrous compositions (equation-30; Putirka, 2008). This model is based on the jadeite-diopside/hedenbergite exchange between clinopyroxene and the associated melt and allows the determination of pressure with SEE ±1.6 kbar. This would produce the most accurate result of all clinopyroxene barometers available (Mollo et al., 2010). For orthopyroxenes we used the thermometer of equation-28a (Putirka, 2008), with SEE ±28 °C and the orthopyroxene barometer for hydrous compositions (equation-29b; Putirka, 2008) with SEE ±2.1 kbar for hydrous systems. For plagioclases we used the model calibrated for hydrous systems that estimates pressure with SEE ±2.47 kbar (equation-25a; Putirka, 2008) and temperature with SEE ±36 °C (eq. 24a; Putirka, 2008). All these P-T estimates were made fixing the water content through iterative calculations.

In order to increase the dataset, we applied the thermobarometers to additional mineral phases of four crystal-poor NdCVC lavas (ca. <10 vol % in phenocrystal content; Table 2) with geochemical data available from the literature (Murphy, 1995). These samples have textural information showing absence or no compositional evidence of magma mixing with relatively homogeneous composition of the phenocrysts in the core and rims. The results show P-T undistinguishable from those yielded by the selected ones. In addition, we include P-T estimates for mineral phases included in a crystal-poor dike (NCH-63; Table 2) and also for clinopyroxene-glass in equilibrium included in a pyroclastic sample (NCH-53). Samples used in the thermobarometric calculations are listed in Table 2, together with the SiO_2 wt%, crystal content and the temperature used for water content estimations for each one. Our analysis encompasses from basaltic andesitic to rhyodacitic compositions, Late Pleistocene to Holocene in age and thus we extrapolate the results to entire lifespan of this volcanic complex.

For clinopyroxenes, calculated P-T range from 918 to 1130 °C and 0.6 to 4.6 kbar. For orthopyroxene the calculated P-T range from 934 to 1069 °C and 3.0 to 5.4 kbar and for plagioclase these values are between 913 and 1088 °C and from 1.2 to 3.9 kbar. In Fig. 7, the calculated P-T values for orthopyroxene, plagioclase and clinopyroxene are plotted together. In addition, with the pressure values and using a density of 2.7 g/cm^3 for the upper crust in this area (Tassara et al., 2006), we estimated the crystallization depth of different mineral phases. In general, the lower crystallization pressures are obtained in mineral phases included in dacites and rhyodacites.

Crystallization pressures of the orthopyroxenes included in dacites and rhyodacites could be overrated. We assume this because plagioclase/orthopyroxene pairs coexist across a wide range of natural melts and should continuously evolve under similar pressure-temperature conditions (Almeev et al., 2013). This is not observed in these samples despite the fact that clinopyroxene, orthopyroxene and plagioclase form crystal clots suggesting that these minerals probably formed simultaneously. On the other hand, the crystallization temperatures calculated for orthopyroxenes, plagioclases and clinopyroxenes are close, since the orthopyroxene-melt thermometer (equation-28a; Putirka, 2008) has a range of applicability that includes these compositions of the melt. Instead, the differences between the pressures of orthopyroxene with the other mineral phases in the dacites and rhyodacites could be due to the fact that, for certain compositions, the orthopyroxene geobarometers presented in Putirka (2008) might not work well, because they have been calibrated using mainly mafic to ultramafic compositions. Histograms for all data and separated by host rock compositions are presented in Fig. 8, in which the crystallization pressures of orthopyroxenes in dacites

Table 2
Samples used in thermobarometric calculations.

Samples[a]	Unit	SiO2 wt%	Crystal content (%)[b]	Temperature (°C)[c]	Average (SEE ±0.35 wt% H_2O)[d]
NCH-31	LTd	67.8	95	930–931	3.0
NCH-37	LTpp	68.0	91	920	3.1
NCH-44	CBg	62.8	93	1012	2.2
NCH-53	P. Cone	56.1	–	–	–
NCH-63	Dyke	57.9	96	1075	2.2
C11	CBcpb	63.0	89	1033	1.9
C29	CBgb	60.2	97	1065	1.7
C44	Pll	58.2	95	1077	1.9
C52	LTv	69.5	89	905	3.3

[a] Samples identified with the prefix C data taken from Murphy (1995).
[b] Normalized to vesicle-free.
[c] The temperature corresponds to the lowest temperature for clinopyroxenes estimated with a thermobarometer independent of the water content (Putirka, 2008 in Putirka, 2008). In NCH-31 the estimated temperature according to the method outlined in Ghiorso and Evans, 2008 with pairs of Fe-Ti oxides in equilibrium is also shown.
[d] Calculated H_2O (wt%) contents using the plagioclase-melt hygrometer proposed by Waters and Lange (2015). Average of the estimates in rim-whole rock pairs. For NCH-53 we used 2.2 H_2O wt%, because plagioclase analysis was not performed in this sample.

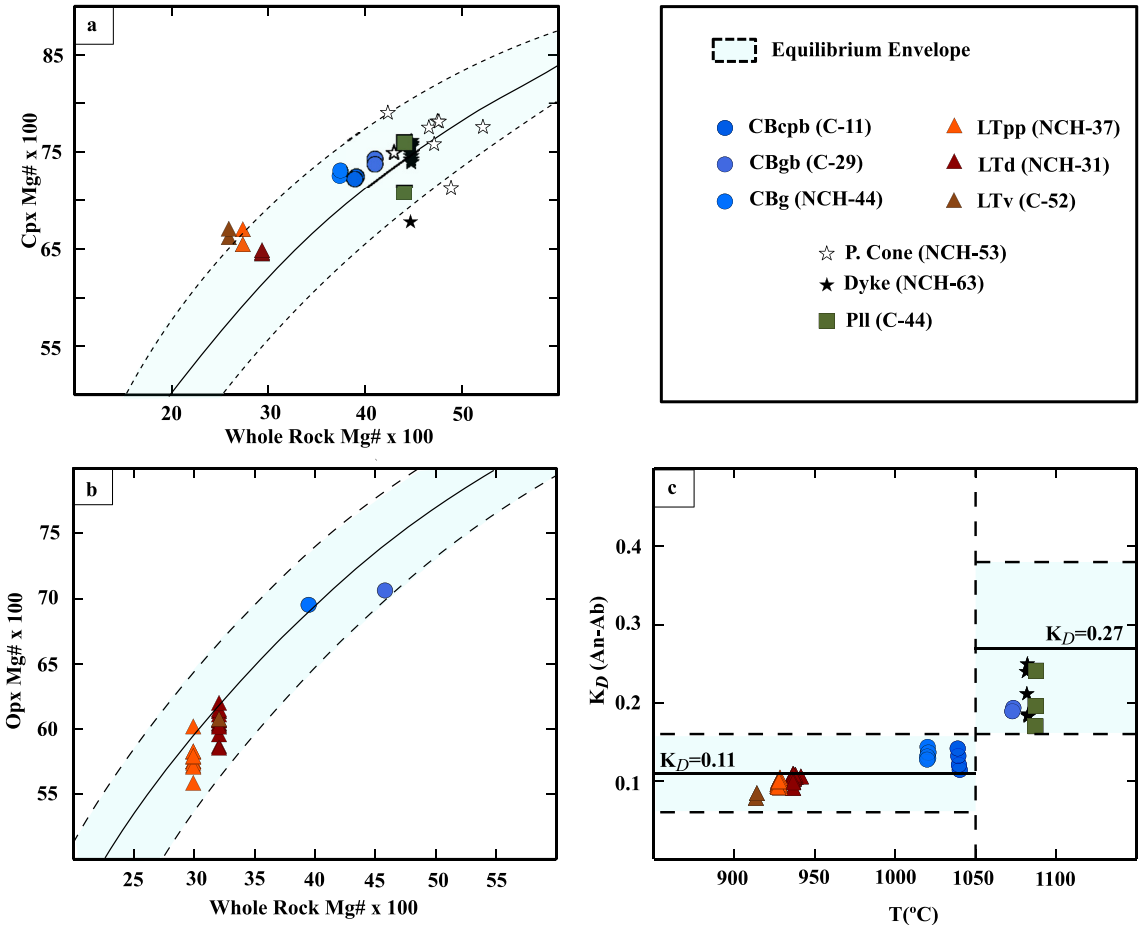

Fig. 6. Mineral-melt equilibrium. Light blue zone shows the equilibrium area for the different minerals. (a) Rhodes diagram to evaluate the equilibrium of clinopyroxenes, Mg# of whole-rock vs Mg# of clinopyroxene. The equilibrium envelope is given by Kd [Fe-Mg] = 0.28 ± 0.8; (b) Rhodes diagram to evaluate the equilibrium of orthopyroxenes, Mg# of whole-rock vs Mg# of orthopyroxenes. The equilibrium envelope is given by Kd [Fe-Mg] = 0.29 ± 0.6; (c) Plagioclase equilibrium test. For T° <1050 °C the equilibrium area is given by Kd [An-Ab] = 0.11 ± 0.5 and for T° >1050 °C the equilibrium envelope is given by Kd [An-Ab] = 0.27 ± 0.11. The Kd ranges between minerals and melt (in this case the whole-rock) are taken from Putirka, 2008. (For interpretation of the references to colour in this figure legend, the reader is referred to the web version of this article.)

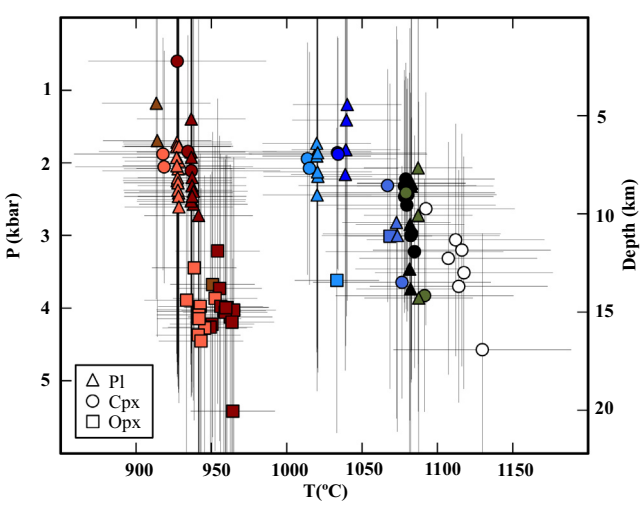

Fig. 7. P-T-Depth diagram. Results for clinopyroxene thermobarometer (Putirka, 2008) with the temperature estimated from Putirka (2003, in Putirka, 2008) and standard error of estimate (SEE) ± 59 °C and pressure (Cpx Eq.30; Putirka, 2008) with SEE ± 1.6 kbar; for plagioclase thermobarometer (Pl Eq.25a SEE ±2.47 kbar, eq. 24a SEE ± 36 °C; Putirka, 2008), and orthopyroxene thermobarometer (Opx Eq.29b SEE ±2.1 kbar, eq. 28a SEE ±28 °C; Putirka, 2008). The depth was estimated with a crustal density of 2.7 g/cm^3. Symbols as in Fig. 6.

and rhyolites and the SEE of thermobarometric calculations do not consider. For all data the depth spans from 2.2 to 16.9 km, with basaltic andesites/andesites from 7.7 to 16.9 km and, dacites/rhyodacites from 2.2 to 9.7 km. These results suggest a vertical compositional zoning in the NdCVC plumbing system.

In order to consider the SEE of the different geobarometers, the data obtained from crystallization pressures (Fig. 8) were treated by means of a Bayesian bootstrap analysis (details in Rubin, 1981). This analysis yielded the most probable value of the mean pressure/depth within a 95% confidence interval. Bayesian bootstraps used the RStudio (RStudio Team, 2020) and the bayesboot package (v0.2.2; Bååth, 2018). Before applying this analysis and due to the limited number of samples, we simulate 50 samples of 1000 data each, with a normal distribution, with the arithmetic mean of our depth and with the SEE from the used geobarometers. After that, the Bayesian bootstrap analysis was performed, where a resampling with 4000 points was carried out for each of the 50 simulated samples. Results for the most probable mean crystallization depth within the 95% confidence for mineral phases included in dacites/rhyodacites ranges from 6.2 to 8.5 km below the Earth surface, and for basaltic andesites/andesites between 9.9 and 11.9 km (Boxplot in Fig. 8).

This statistical analysis would confirm a compositional zonation of the plumbing system, at least in the Cerro Blanco edifice. In Las Termas edifice, field-based evidence as to the presence of basaltic andesitic enclaves in some dacites and rhyodacites, suggest a similar configuration of the plumbing system. On the other hand, P-T estimates of pre-caldera lavas

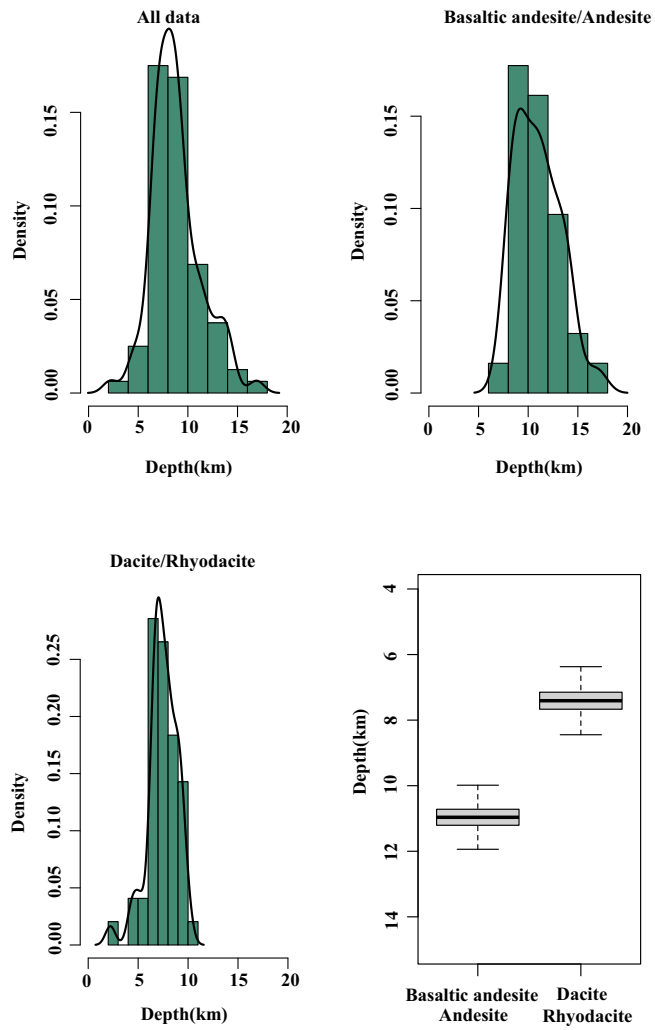

Fig. 8. Histograms and boxplot. Histograms with the depth of crystallization for different host rock compositions (density curve with black line) and Boxplot (Confidence Interval: 95%; center line, median; box limits, upper and lower quartiles; whiskers, 1.5 times interquartile range) with the mean of the most probable crystallization depths according to host rock composition.

(C-44, Pll) and a dyke that cuts this unit (NCH-63) suggests that at least the deepest determined level of the plumbing system has been stable since Late Pleistocene.

5. Discussion

5.1. Vertical zonation of the plumbing system

Within uncertainties, pressure estimations unravel a plumbing system that extends vertically from 2.2 to 16.9 km below the Nevados de Chillán Volcanic Complex. This plumbing system seems to be compositionally zoned in the vertical dimension, as also observed for other volcanic systems of the SVZ (e.g., Gilbert et al., 2012; Ruprecht et al., 2012) and elsewhere (e.g., Samaniego et al., 2020; Giacomoni et al., 2016). This zonation is consistent with the most accepted view that more evolved magmas, when structurally trapped at upper crustal levels, would act as density filters for less evolved magmas reaching from deeper levels of the crust (e.g., Eichelberger, 2010).

5.2. Relating the plumbing system with crustal discontinuities

Factors controlling magma storage at depth are multiple and their interplay is still controversial (e.g., Valentine and Krogh, 2006; Kavanagh et al., 2006; Menand, 2008). Density contrast between the uprising magmas and continental crust is an important factor producing large scale filters (Eichelberger, 2010), which is in turn modulated by the local stress regime (e.g., Gudmundsson, 2011; Sparks and Cashman, 2017) and the internal stratification of the plumbing system. We use the Fig. 9 to show the possible role played by the crustal architecture underneath NdCVC in controlling the observed vertical zonation of the plumbing system. We explore in Fig. 9 the relationship between our estimated crystallization depths and the geophysically-constrained structure of the subduction zone at the latitude of NdCVC. Particularly, Fig. 9a is an EW cross-section at 36.85°S showing the geometries of four major discontinuities (slab upper surface, lithosphere-astenosphere boundary (LAB), Moho and intracrustal Conrad discontinuity (ICD)) extracted from the 3D model of Tassara and Echaurren (2012). This is a continental-scale representation of the mass distribution underneath the Andean margin that was created performing a forward modeling of gravity anomalies and using different sources of seismic data as constraint (Tassara et al., 2006; Tassara and Echaurren, 2012). Also shown are contours of the Vs seismic noise model of González-Vidal et al. (2018) that are expressed as the variation of Vs with respect to its absolute mean value at a given depth (dVs/Vs x 100%).

Outside the volcanic arc region, we note a general coincidence between the contour line for dVs/Vs = −3% and the depth of the ICD, which separates the light (density $\rho = 2.7$ g/cm^3) upper crust from a dense ($\rho = 3.1$ g/cm^3) lower crust. This demonstrates that both independently obtained geophysical images are tied to the underlying crustal structure, with the ICD reflecting the structural contact between crustal layers. The mid-lower crust beneath the volcanic arc is characterized by an anomalously low Vs region, pointing to high temperatures probably related to a vertical transport of magma from a MASH zone (melting, assimilation, storage and homogenization). Fig. 9b represents the plumbing system below NdCVC over a lithosphere marked by four discontinuities modeled by Tassara and Echaurren (2012) and the crystallization depths that we estimated for the two different compositional ranges in Fig. 8. The most important feature of this scheme is that magmas transported from the MASH zone throughout the mid-lower crust are accumulated underneath the ICD, where they partially differentiated to produce a basaltic andesitic and andesitic magmas. The further differentiation of this magma by fractional crystallization generates a lighter melt that ascend above the ICD and then produces the more evolved dacitic/rhyodacitic magma characterizing the upper level of the system. Thus, the ICD seems to represent a fundamental discontinuity of the plumbing system, separating a deep intermediate-to-basic reservoir from an evolved zone.

Fig. 9c compares the NdCVC lithospheric column and magmatic plumbing system with the structure and crystallization depths proposed for other volcanic systems of the SVZ that have been studied with similar petrological techniques (e.g., Costa et al., 2004; Gilbert et al., 2012; Ruprecht et al., 2012; Castro et al., 2013; Morgado et al., 2019; Vander Auwera et al., 2019). Latitudinal variations in the depth to the LAB and Moho reflects first-order differences in the deep crustal and lithospheric structure along the SVZ, which has been shown as an influence in the nature of primitive magmas reaching the MASH zone (e.g., Hildreth and Moorbath, 1988; Völker et al., 2011). Despite the differences and spatial variations of the ICD that are likely related to differences in the geologically-controlled upper crustal structure (Tassara et al., 2006), we note that all the compared volcanic systems developed a vertical zonation that is similar to NdCVC in that evolved and mafic compositions seem to be separated by the ICD. Indeed, all the estimated depths for the crystallization of intermediate-to-evolved magmas lies above the local ICD, whereas the roof of the depth ranges where intermediate-to-mafic magmas crystallize approach this intracrustal discontinuity.

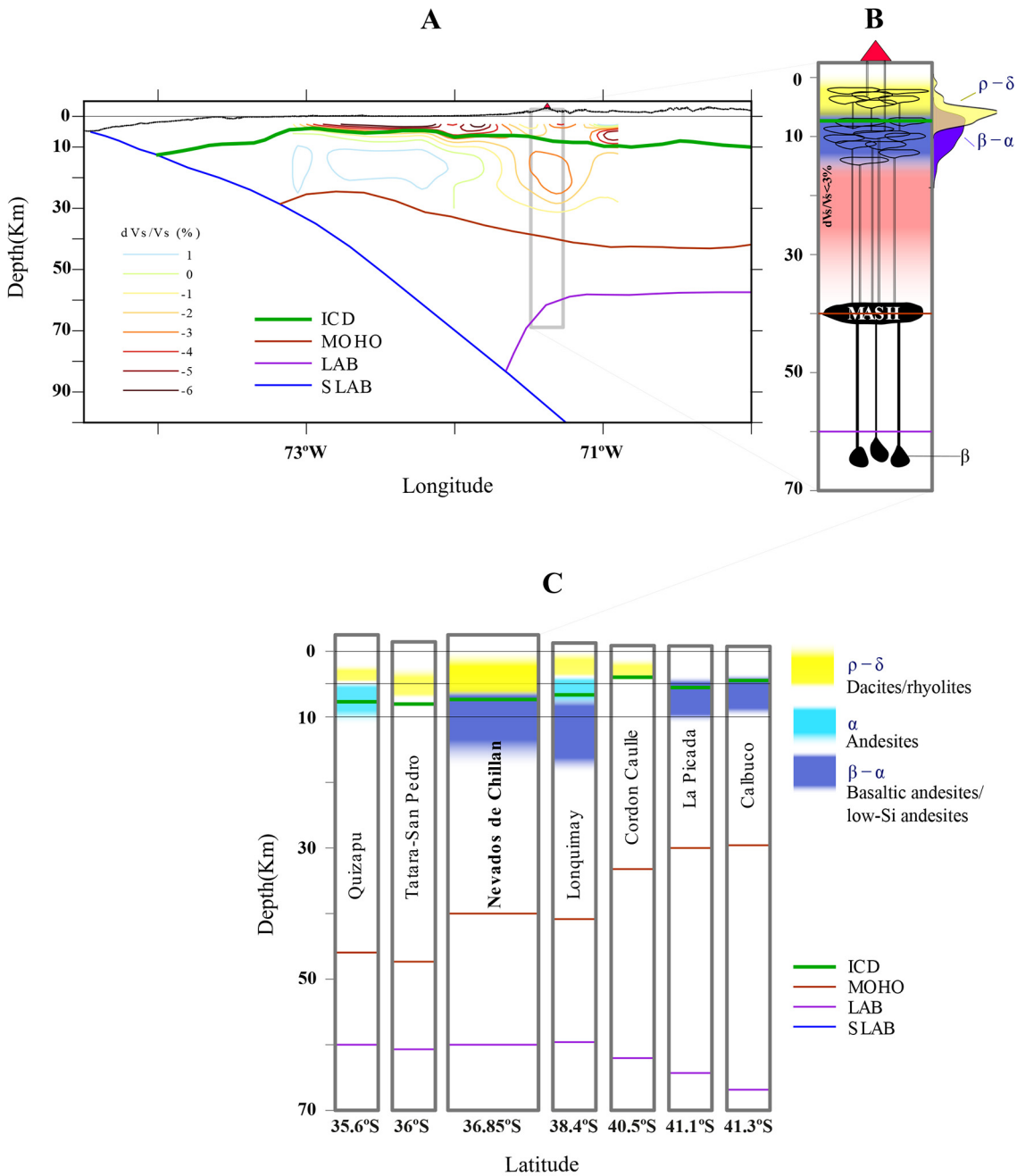

Fig. 9. A) Lithospheric-scale structure of the Andean subduction zone at the latitude of NdCVC (36.85°S) as derived from the model of Tassara and Echaurren (2012). This model defines the geometries (depth w/r to sea level) of the subducted slab upper surface (SLAB), lithosphere-asthenosphere boundary (LAB), crust-mantle boundary (MOHO) and intracrustal Conrad discontinuity (ICD). Colored contours are extracted from the ambient seismic noise model of González-Vidal et al. (2018) and show lines of equal Vs anomaly (dVs) as expressed in percentage with respect to the average value of Vs at a given depth range. The position of NdCVC is marked with a red triangle on top of the topographic profile. B) Representative lithospheric column below NdCVC highlighting the main structural features extracted from A and our estimated ranges of crystallization depths for dacites/rhyodacites (ρ-δ) and basaltic andesites-andesites (β-α), as informed in Fig. 8 (depth w/r to Earth surface, right-hand side of the column). We draw here a schematic representation of the magmatic plumbing system that includes a region of asthenospheric partial melting below the LAB where primitive basalts (β) are created; a MASH zone at the MOHO where these basalts are trapped; dikes transporting basalts homogenized in this zone to a mid-crust reservoir formed by coalescent sills below the ICD where basaltic-andesitic magmas crystalize and differentiates forming more evolved magmas that ascent by dikes to an upper crustal reservoir located above the ICD C) Comparison between the lithospheric structure (Tassara and Echaurren, 2012) and compositional zonation of magmatic plumbing systems underneath several volcanoes of the Southern Volcanic Zone where petrological studies similar to our approach have been published. (For interpretation of the references to colour in this figure legend, the reader is referred to the web version of this article.)

6. Conclusions

Our thermobarometric results suggest that the NdCVC plumbing system extends vertically from 2.2 to 16.9 km. This architecture would have persisted over time without significant variations in the crystallization depth range throughout the Late Pleistocene-Holocene evolution of NdCVC, at least in terms of the lowest boundary. The depth of crystallization for mineral phases included in basaltic andesites/andesites extends beneath the intracrustal Conrad discontinuity in this area while evolved magmas migrate and store above this level, which depicts a compositionally zoned plumbing system. Our results highlight the first-order role that crustal

geological discontinuities may play in the long-term configuration of a plumbing system.

Funding

This work was funded by Chilean Fondecyt Project (1151175, Andrés Tassara as PI).

Andrés Oyarzún was supported by Conicyt PhD Fellowship (21191951) and Universidad de Concepción Fellowship.

Declaration of Competing Interest

The authors declare that they have no known competing financial interests or personal relationships that could have appeared to influence the work reported in this paper.

Acknowledgements

The authors grateful to Laura Hernández (GEA, Universidad de Concepción, Chile) who provided effective assistance in EPMA. The use of the EPMA facility at the Department of Earth Science, Rice University, Houston, TX is kindly acknowledged. We thank Francisco Ríos for assisting with the statistical analysis and to Nicolás Luengo for providing us with the sample NCH-55. We also thank Dr. Heidi Wehrmann for the use of chemical data (clinopyroxene and glass included in tephra samples) obtained at the Universidad de Concepción summer school (2017). We thank to both anonymous reviewers for their criticism that certainly improved the manuscript.

Appendix A. Supplementary data

Supplementary data to this article can be found online at https://doi.org/10.1016/j.jvolgeores.2021.107455.

References

Aiuppa, A., Cannata, A., Cannavò, F., Di Grazia, G., Ferrari, F., Giudice, G., Gurrieri, S., Liuzzo, M., Mattia, M., Montalto, P., Patanè, D., Puglisi, G., 2010. Patterns in the recent 2007–2008 activity of Mount Etna volcano investigated by integrated geophysical and geochemical observations. Geochem. Geophys. Geosyst. 11 (9). https://doi.org/10.1029/2010GC003168.

Almeev, R.R., Kimura, J.I., Ariskin, A.A., Ozerov, A.Y., 2013. Decoding crystal fractionation in calc-alkaline magmas from the Bezymianny Volcano (Kamchatka, Russia) using mineral and bulk rock compositions. J. Volcanol. Geotherm. Res. 263, 141–171. https://doi.org/10.1016/j.jvolgeores.2013.01.003.

Andújar, J., Scaillet, B., Pichavant, M., Druitt, T.H., 2015. Differentiation conditions of a basaltic magma from Santorini, and its bearing on the production of andesite in arc settings. J. Petrol. 56 (4), 765–794. https://doi.org/10.1093/petrology/egv016.

Annen, C., Sparks, R.S.J., 2002. Effects of repetitive emplacement of basaltic intrusions on thermal evolution and melt generation in the crust. Earth Planet. Sci. Lett. 203 (3–4), 937–955. https://doi.org/10.1016/S0012-821X(02)00929-9.

Annen, C., Blundy, J.D., Leuthold, J., Sparks, R.S.J., 2015. Construction and evolution of igneous bodies: Towards an integrated perspective of crustal magmatism. Lithos. 230, 206–221. https://doi.org/10.1016/j.lithos.2015.05.008.

Bååth, R., 2018. Bayesboot: An Implementation of Rubin's (1981) Bayesian Bootstrap. R Package Version 0.2.2. https://CRAN.R-project.org/package=bayesboot.

Bacon, C.R., Hirschmann, M.M., 1988. Mg/Mn partitioning as a test for equilibrium between coexisting Fe-Ti oxides. Am. Mineral. 73 (1–2), 57–61.

Bas, M.L., Maitre, R.L., Streckeisen, A., Zanettin, B., Subcommission, I.U.G.S., on the Systematics of Igneous Rocks, 1986. A chemical classification of volcanic rocks based on the total alkali-silica diagram. J. Petrol. 27 (3), 745–750.

Benet, D., Costa, F., Pedreros, G., Cardona, C., 2021. The volcanic ash record of shallow magma intrusion and dome emplacement at Nevados de Chillán Volcanic complex, Chile. J. Volcanol. Geotherm. Res. 107308. https://doi.org/10.1016/j.jvolgeores.2021.107308.

Blundy, J., Cashman, K., 2001. Ascent-driven crystallisation of dacite magmas at Mount St Helens, 1980–1986. Contrib. Mineral. Petrol. 140 (6), 631–650.

Cardona, C., Gil-Cruz, F., Franco-Marín, L., San Martín, J., Valderrama, O., Lazo, J., Cartes, C., Morales, S., Hernández, E., Quijada, J., Pinto, C., Vidal, M., Bravo, C., Pedreros, G., Contreras, M., Figueroa, M., Córdova, L., Mardones, C., Alarcón, A., Velásquez, G., Bucarey, C., 2021. Volcanic activity accompanying the emplacement of dacitic lava domes and effusion of lava flows at Nevados de Chillán Volcanic Complex–Chilean Andes (2012 to 2020). J. Volcanol. Geotherm. Res., 107409 https://doi.org/10.1016/j.jvolgeores.2021.107409.

Castro, J.M., Schipper, C.I., Mueller, S.P., Militzer, A.S., Amigo, A., Parejas, C.S., Jacob, D., 2013. Storage and eruption of near-liquidus rhyolite magma at Cordón Caulle, Chile. Bull. Volcanol. 75 (4), 1–17. https://doi.org/10.1007/s00445-013-0702-9.

Cembrano, J., Lara, L., 2009. The link between volcanism and tectonics in the southern volcanic zone of the Chilean Andes: a review. Tectonophysics. 471 (1–2), 96–113. https://doi.org/10.1016/j.tecto.2009.02.038.

Coppola, D., Laiolo, M., Lara, L.E., Cigolini, C., Orozco, G., 2016. The 2008 "silent" eruption of Nevados de Chillán (Chile) detected from space: Effusive rates and trends from the MIROVA system. J. Volcanol. Geotherm. Res. 327, 322–329. https://doi.org/10.1016/j.jvolgeores.2016.08.016.

Costa, F., Scaillet, B., Pichavant, M., 2004. Petrological and experimental constraints on the pre-eruption conditions of Holocene dacite form Volcán San Pedro (36° S, Chilean Andes) and the importance of Sulphur in silicic subduction-related magmas. J. Petrol. 45 (4), 855–881. https://doi.org/10.1093/petrology/egg114.

Deruelle, B., López-Escobar, L., 1999. Basalts, andesites, dacites and rhyolites from Nevados de Chillán and Antuco stratovolcanoes (Southern Andes): A remarkable example of magmatic differentiation through crystal fractionation. Comp. Rend. Acad. Sci. Paris Ser. 2A (329), 337–344.

Dixon, H.J., Murphy, M.D., Sparks, S.J., Chávez, R., Naranjo, J.A., Dunkley, P.N., Young, S.R., Gilbert, J.S., Pringle, M.R., 1999. The geology of Nevados de Chillán volcano, Chile. Rev. Geol. Chile 26 (2), 227–253. https://doi.org/10.4067/S0716-02081999000200006.

Eichelberger, J., 2010. Messy magma mixtures. Nat. Geosci. 3 (9), 593–594. https://doi.org/10.1038/ngeo951.

Folguera, A., Zapata, T., Ramos, V.A., 2006. Late Cenozoic extension and the evolution of the Neuquén Andes. Spec. Pap. Geol. Soc. Am. 407, 267.

Ghiorso, M.S., Evans, B.W., 2008. Thermodynamics of rhombohedral oxide solid solutions and a revision of the Fe-Ti two-oxide geothermometer and oxygen-barometer. Am. J. Sci. 308 (9), 957–1039. https://doi.org/10.2475/09.2008.01.

Giacomoni, P.P., Coltorti, M., Bryce, J.G., Fahnestock, M.F., Guitreau, M., 2016. Mt. Etna plumbing system revealed by combined textural, compositional, and thermobarometric studies in clinopyroxenes. Contrib. Mineral. Petrol. 171 (4), 34.

Gilbert, D., Freundt, A., Kutterolf, S., Burkert, C., 2012. Post-glacial time series of explosive eruptions and associated changes in the magma plumbing system of Lonquimay volcano, south Central Chile. Int. J. Earth Sci. 103 (7), 2043–2062. https://doi.org/10.1007/s00531-012-0796-x.

Ginibre, C., Kronz, A., WoÈrner, G., 2002. High-resolution quantitative imaging of plagioclase composition using accumulated backscattered electron images: new constraints on oscillatory zoning. Contrib. Mineral. Petrol. 142 (4), 436–448. https://doi.org/10.1007/s004100100298.

González, O., Vergara, M., 1962. Reconocimiento Geológico de la cordillera de los Andes entre los paralelos 35° y 38°S. 24. Universidad de Chile, Instituto de Geología Publicacion, p. 121.

González-Vidal, D., Obermann, A., Tassara, A., Bataille, K., Lupi, M., 2018. Crustal model of the Southern Central Andes derived from ambient seismic noise Rayleigh-wave tomography. Tectonophysics. 744, 215–226. https://doi.org/10.1016/j.tecto.2018.07.004.

Gudmundsson, A., 2011. Deflection of dykes into sills at discontinuities and magma-chamber formation. Tectonophysics. 500 (1–4), 50–64. https://doi.org/10.1016/j.tecto.2009.10.015.

Hernando, I.R., Llambías, E.J., González, P.D., Sato, K., 2012. Estratigrafía volcánica y evidencia de mezcla de magmas en el volcán Payún Matrú del Cuaternario, en el retroarco andino de Argentina occidental. Andean Geol. 39 (1), 158–179.

Hildreth, W., Moorbath, S., 1988. Crustal contributions to arc magmatism in the Andes of Central Chile. Contrib. Mineral. Petrol. 98 (4), 455–489. https://doi.org/10.1007/BF00372365.

Humphreys, M.C., Blundy, J.D., Sparks, R.S.J., 2006. Magma evolution and open-system processes at Shiveluch Volcano: insights from phenocryst zoning. J. Petrol. 47 (12), 2303–2334. https://doi.org/10.1093/petrology/egl045.

Kahl, M., Chakraborty, S., Costa, F., Pompilio, M., 2011. Dynamic plumbing system beneath volcanoes revealed by kinetic modeling, and the connection to monitoring data: an example from Mt. Etna. Earth Planet. Sci. Lett. 308 (1–2), 11–22. https://doi.org/10.1016/j.epsl.2011.05.008.

Kavanagh, J.L., Menand, T., Sparks, R.S.J., 2006. An experimental investigation of sill formation and propagation in layered elastic media. Earth Planet. Sci. Lett. 245 (3–4), 799–813. https://doi.org/10.1016/j.epsl.2006.03.025.

Lara, L.E., Flores, F., Calderón, R., Cardona, C., 2021. Volcano hazards and risks in Chile. Forecasting and Planning for Volcanic Hazards, Risks, and Disasters. Elsevier, pp. 617–633 https://doi.org/10.1016/B978-0-12-818082-2.00017-2.

López-Escobar, L., Kilian, R., Kempton, P.D., Tagiri, M., 1993. Petrography and geochemistry of Quaternary rocks from the Southern Volcanic Zone of the Andes between 41 30′ and 46 00′S, Chile. Andean Geol. 20 (1), 33–55. https://doi.org/10.5027/andgeoV20n1-a04.

Mee, K., 2004. The Use of Volcanic Facies as Tools for Reconstructing Former Erupting Environments at Nevados de Chillán volcano, Chile. Ph.D. ThesisLancaster University, Lancaster, United Kingdom.

Mee, K., Gilbert, J.S., McGarvie, D.W., Naranjo, J.A., Pringle, M.S., 2009. Palaeoenvironment reconstruction, volcanic evolution and geochronology of the Cerro Blanco subcomplex, Nevados de Chillán volcanic complex, Central Chile. Bull. Volcanol. 71 (8), 933–952. https://doi.org/10.1007/s00445-009-0277-7.

Menand, T., 2008. The mechanics and dynamics of sills in layered elastic rocks and their implications for the growth of laccoliths and other igneous complexes. Earth Planet. Sci. Lett. 267 (1–2), 93–99. https://doi.org/10.1016/j.epsl.2007.11.043.

Middlemost, E.A., 1989. Iron oxidation ratios, norms and the classification of volcanic rocks. Chem. Geol. 77 (1), 19–26. https://doi.org/10.1016/0009-2541(89)90011-9.

Mollo, S., Del Gaudio, P., Ventura, G., Iezzi, G., Scarlato, P., 2010. Dependence of clinopyroxene composition on cooling rate in basaltic magmas: Implications for

thermobarometry. Lithos. 118 (3–4), 302–312. https://doi.org/10.1016/j.lithos.2010.05.006.

Morgado, E., Morgan, D.J., Harvey, J., Parada, M.Á., Castruccio, A., Brahm, R., Gutiérrez, F., Georgiev, B., Hammond, S.J., 2019. Localised heating and intensive magmatic conditions prior to the 22–23 April 2015 Calbuco volcano eruption (Southern Chile). Bull. Volcanol. 81 (4), 1–21. https://doi.org/10.1007/s00445-019-1280-2.

Moussallam, Y., Bani, P., Schipper, C.I., Cardona, C., Franco, L., Barnie, T., Amigo, A., Curtis, A., Peters, N., Aiuppa, A., Giudice, G., Oppenheimer, C., 2018. Unrest at the Nevados de Chillán volcanic complex: a failed or yet to unfold magmatic eruption? Volcanica. https://doi.org/10.30909/vol.01.01.1932.

Murphy, M.D., 1995. The Geology and Geochemistry of Nevados de Chillán Volcano. ChileBritish Geological Survey, Keyworth, Nottingham, U.K.

Naranjo, J.A., Lara, L.E., 2004. August-September 2003 small vulcanian eruption at the Nevados de Chillán Volcanic complex (36° 50'S), Southern Andes (Chile). Rev. Geol. Chile 31 (2), 359–366. https://doi.org/10.4067/S0716-02082004000200011.

Naranjo, J.A., Gilbert, J., Sparks, R.S., 2008. Geología del complejo volcánico Nevados de Chillán, Región del Biobío. Servicio Nacional de Geología y Minería, Carta Geológica de Chile, Serie Geología Básica. 114, p. 28 1 mapa escala 1:50.000.

Nelson, S.T., Montana, A., 1992. Sieve-textured plagioclase in volcanic rocks produced by rapid decompression. Am. Mineral. 77 (11−12), 1242–1249.

Putirka, K.D., 2008. Thermometers and barometers for volcanic systems. Rev. Mineral. Geochem. 69 (1), 61–120. https://doi.org/10.2138/rmg.2008.69.3.

Radic, J.P., 2010. Las cuencas cenozoicas y su control en el volcanismo de los Complejos Nevados de Chillán y Copahue-Callaqui (Andes del Sur, 36-39 S). Andean Geol. 37 (1), 220–246.

Radic, J.P., Sipetrol, S.A., 2006. Anisotropías de basamento como control estructural del volcanismo en el Complejo volcánico Chillán (Andes del Sur, 36 S). XI Congreso Geológico Chileno, Antofagasta. p. Actas. 2.

Rhodes, J.M., Dungan, M.A., Blanchard, D.P., Long, P.E., 1979. Magma mixing at mid-ocean ridges: evidence from basalts drilled near 22 N on the Mid-Atlantic Ridge. Tectonophysics. 55 (1–2), 35–61. https://doi.org/10.1016/0040-1951(79)90334-2.

RStudio Team, 2020. RStudio: Integrated Development for R. RStudio, PBC, Boston, MA URL http://www.rstudio.com/.

Rubin, D.B., 1981. The bayesian bootstrap. Ann. Stat. 130–134.

Ruprecht, P., Bergantz, G.W., Cooper, K.M., Hildreth, W., 2012. The crustal magma storage system of Volcán Quizapu, Chile, and the effects of magma mixing on magma diversity. J. Petrol. 53 (4), 801–840. https://doi.org/10.1093/petrology/egs002.

Ruprecht, P., Simon, A.C., Fiege, A., 2020. The survival of mafic enclaves and the timing of magma recharge. Geophys. Res. Lett. 47 (14), e2020GL087186. https://doi.org/10.1029/2020GL087186.

Samaniego, P., Rivera, M., Manrique, N., Schiavi, F., Nauret, F., Liorzou, C., Ancellin, M.A., 2020. Linking magmatic processes and magma chemistry during the post-glacial to recent explosive eruptions of Ubinas volcano (southern Peru). J. Volcanol. Geotherm. Res. 407, 107095. https://doi.org/10.1016/j.jvolgeores.2020.107095.

Sigmundsson, F., Parks, M., Pedersen, R., Jónsdóttir, K., Ófeigsson, B.G., Grapenthin, R., Dumont, S., Einarsson, P., Drouin, V., Heimisson, E., Hjasrtardóttir, A., Gudmunsson, M., Geirsson, H., Hreinsdóttir Sturkell, E., Hooper, A., Högnadóttir Vogfjörd, K., Barnie, T., Roberts, M.J., 2018. Magma movements in volcanic plumbing systems and their associated ground deformation and seismic patterns. Volcanic and Igneous Plumbing Systems. Elsevier, pp. 285–322 https://doi.org/10.1016/B978-0-12-809749-6.00011-X.

Sisson, T.W., Grove, T.L., 1993. Temperatures and H 2 O contents of low-MgO high-alumina basalts. Contrib. Mineral. Petrol. 113 (2), 167–184. https://doi.org/10.1007/BF00283225.

Søager, N., Holm, P.M., Llambías, E.J., 2013. Payenia volcanic province, southern Mendoza, Argentina: OIB mantle upwelling in a backarc environment. Chem. Geol. 349, 36–53. https://doi.org/10.1016/j.chemgeo.2013.04.007.

Sparks, R.S.J., Cashman, K.V., 2017. Dynamic magma systems: implications for forecasting volcanic activity. Elements. 13 (1), 35–40. https://doi.org/10.2113/gselements.13.1.35.

Stanton-Yonge, A., Griffith, W.A., Cembrano, J., St. Julien, R., Iturrieta, P., 2016. Tectonic role of margin-parallel and margin-transverse faults during oblique subduction in the southern volcanic zone of the Andes: insights from boundary element modeling. Tectonics. 35 (9), 1990–2013. https://doi.org/10.1002/2016TC004226.

Stern, C.R., 2004. Active Andean volcanism: its geologic and tectonic setting. Rev. Geol. Chile 31 (2), 161–206. https://doi.org/10.4067/S0716-02082004000200001.

Tassara, A., Echaurren, A., 2012. Anatomy of the Andean subduction zone: three-dimensional density model upgraded and compared against global-scale models. Geophys. J. Int. 189 (1), 161–168. https://doi.org/10.1111/j.1365-246X.2012.05397.x.

Tassara, A., Götze, H.J., Schmidt, S., Hackney, R., 2006. Three-dimensioal density model of the Nazca plate and the Andean continental margin. J. Geophys. Res. Solid Earth 111 (B9). https://doi.org/10.1029/2005JB003976.

Tepley III, F.J., Davidson, J.P., Clynne, M.A., 1999. Magmatic interactions as recorded in plagioclase phenocrysts of Chaos Crags, Lassen Volcanic Center, California. J. Petrol. 40 (5), 787–806. https://doi.org/10.1093/petroj/40.5.787.

Tsuchiyama, A., 1985. Dissolution kinetics of plagioclase in the melt of the system diopside-albite-anorthite, and origin of dusty plagioclase in andesites. Contrib. Mineral. Petrol. 89 (1), 1–16. https://doi.org/10.1007/BF01177585.

Valentine, G.A., Krogh, K.E., 2006. Emplacement of shallow dikes and sills beneath a small basaltic volcanic center–the role of pre-existing structure (Paiute Ridge, southern Nevada, USA). Earth Planet. Sci. Lett. 246 (3–4), 217–230. https://doi.org/10.1016/j.epsl.2006.04.031.

Vander Auwera, J., Namur, O., Dutrieux, A., Wilkinson, C.M., Ganerod, M., Coumont, V., Bolle, O., 2019. Mantle melting and magmatic processes under La Picada stratovolcane (CSVZ, Chile). J. Petrol. 60 (5), 907–944. https://doi.org/10.1093/petrology/egz020.

Varela, J., Moreno, H., 1982. Los Depósitos de Relleno de la Depresión Central de Chile entre los ríos Lontué y Bío-Bío. III Congreso Geológico Chileno, Actas. 2, pp. F280–F306.

Vergara, M., Muñoz, J., 1982. La Formación Cola de Zorro en la alta cordillera Andina Chilena (36–39 Lat. S), sus características petrográficas y petrológicas: Una revisión. Rev. Geol. Chile 17 (1), 31–46.

Völker, D., Kutterolf, S., Wehrmann, H., 2011. Comparative mass balance of volcanic edifices at the southern volcanic zone of the Andes between 33 S and 46 S. J. Volcanol. Geotherm. Res. 205 (3–4), 114–129. https://doi.org/10.1016/j.jvolgeores.2011.03.011.

Waters, L.E., Lange, R.A., 2015. An updated calibration of the plagioclase-liquid hygrometer-thermometer applicable to basalts through rhyolites. Am. Mineral. 100 (10), 2172–2184. https://doi.org/10.2138/am-2015-5232.

Zellmer, G.F., Turenr, S.P., 2007. Arc dacite genesis pathways: evidence from mafic enclaves and their hosts in Aegean lavas. Lithos. 95 (3–4), 346–362. https://doi.org/10.1016/j.lithos.2006.08.002.